Available online at www.sciencedirect.com
ScienceDirect
Journal of Computational Physics 222 (2007) 654–672
JOURNAL OF COMPUTATIONAL PHYSICS
www.elsevier.com/locate/jcp

# Simulations of reactive transport and precipitation with smoothed particle hydrodynamics

Alexandre M. Tartakovsky [a,*], Paul Meakin [b], Timothy D. Scheibe [a], Rogene M. Eichler West [a]

[a] *Pacific Northwest National Laboratory, P.O. Box 999, Richland, WA 99352, USA*
[b] *Idaho National Laboratory, P.O. Box 1625, MS 2211, Idaho Falls, ID 83415-2211, USA*

Received 7 October 2005; received in revised form 11 July 2006; accepted 15 August 2006
Available online 13 October 2006

**Abstract**

A numerical model based on smoothed particle hydrodynamics (SPH) was developed for reactive transport and mineral precipitation in fractured and porous materials. Because of its Lagrangian particle nature, SPH has several advantages for modeling Navier–Stokes flow and reactive transport including: (1) in a Lagrangian framework there is no non-linear term in the momentum conservation equation, so that accurate solutions can be obtained for momentum dominated flows and; (2) complicated physical and chemical processes such as surface growth due to precipitation/dissolution and chemical reactions are easy to implement. In addition, SPH simulations explicitly conserve mass and linear momentum. The SPH solution of the diffusion equation with fixed and moving reactive solid–fluid boundaries was compared with analytical solutions, Lattice Boltzmann [Q. Kang, D. Zhang, P. Lichtner, I. Tsimpanogiannis, Lattice Boltzmann model for crystal growth from supersaturated solution, Geophysical Research Letters, 31 (2004) L21604] simulations and diffusion limited aggregation (DLA) [P. Meakin, Fractals, scaling and far from equilibrium. Cambridge University Press, Cambridge, UK, 1998] model simulations. To illustrate the capabilities of the model, coupled three-dimensional flow, reactive transport and precipitation in a fracture aperture with a complex geometry were simulated.


*Keywords:* Smoothed particle hydrodynamics; Miscible flow; Reactive transport; Mineral precipitation; Fractures

## 1. Introduction

Numerical solution of the Navier–Stokes equation in domains with complex boundaries that dynamically change as a result of geochemical and/or biochemical processes such as mineral precipitation or biofilm growth presents a very serious challenge to grid-based methods. A number of alternative approaches have been developed for modeling pore-scale reactive transport [1–3]. These models use Lattice Boltzmann (LB) methods to simulate fluid behavior and cellular-automata models to simulate evolution of the boundaries

* Corresponding author. Tel.: +1 509 372 6185.
*E-mail address:* alexandre.tartakovsky.@pnl.gov (A.M. Tartakovsky).

0021-9991/$ - see front matter 
doi:10.1016/j.jcp.2006.08.013

of the flow domain. Some of these models also use LB methods to simulate the diffusion of dissolved materials [1,2]. Another approach is to use grid-based methods to solve the diffusion equation instead of LB simulations, which become unstable for large diffusion coefficients [3]. Pore-scale models based on simplified geometric representations of porous media (such as pore-network models that treat porous materials as a network of linear tubes connecting spherical pore junctions) have also been successfully used to model non-reactive transport in porous media and estimate transport properties such as a dispersion coefficient (e.g. [4–6]). However, extension of pore-network models to simulate reactive transport coupled with mineral precipitation and/or biofilm growth may be problematic because such processes are strongly controlled by pore geometry details.

This paper presents a Lagrangian particle approach based on smoothed particle hydrodynamics (SPH). This approach uses the same particle discretization of a computational domain to solve both the flow and diffusion equations, and to model surface growth as a result of mineral precipitation. Consequently, numerical implementation of the SPH model may be easier than coupled LB-finite element cellular automata growth models. SPH shares with LB the advantages of explicitly conserving mass and linear momentum, and not requiring explicit interface tracking so that geometrically complex and/or dynamic boundaries can be handled without undue difficulty. The Lagrangian particle nature of SPH allows physical and chemical effects to be incorporated into the modeling of flow processes with relatively little code-development effort. In addition, SPH is manifestly Galilean invariant because particle–particle interactions depend on relative particle positions and velocity differences. In a Lagrangian framework, there is no non-linear term in the momentum conservation equation, so that SPH allows accurate solution of momentum dominated flows. In addition, in a Lagrangian framework the mass of solute carried by fluid particles remains constant in the absence of molecular diffusion, so there is no numerical diffusion associated with the discretization of the advective term that is present in a Eulerian framework.

SPH was first introduced by Lucy [7] and Gingold and Monaghan [8] to simulate fluid dynamics in the context of astrophysical applications. Since its introduction, SPH has been successfully used to model a wide range of fluid flow processes and the behavior of solids subjected to large deformations including high energy explosions [9], free surface flows such as dam collapse [10], unsaturated flow in fractures [11,12], flow and non-reactive transport through porous and fractured media [13–17] and flows with homogeneous reactions in an opposed jet burner [18].

The work described in this paper is based on an SPH model for miscible non-reactive flow developed by Tartakovsky and Meakin [17]. Two main modifications were made: (1) reaction term representing a heterogeneous (surface) chemical reaction was added to the SPH diffusion equation; and (2) a new model for solid phase growth and/or dissolution was developed and coupled with SPH simulation of flow and diffusion. In the SPH model, surface reactions are implemented through solid-particle–fluid-particle interconversion. This allows surface reaction at the geometrically complex time dependent boundaries to be simulated without employing complicated front tracking schemes. The boundary evolution (growth and/or dissolution) is modeled by tracking the changes in the masses of the solid particles resulting from precipitation/dissolution reactions. The accuracy of the model was verified by quantitative comparison of two-dimensional numerical results with analytical solutions and qualitative comparisons with Lattice Bolzmann simulations [19]. Finally, three-dimensional reactive flow through and precipitation within a fracture aperture bounded by fractal surfaces was simulated. The results illustrate that the SPH model for reactive transport could be a valuable tool for studying complex coupled hydro-chemical processes in fractured and porous materials.

## 2. SPH transport equations

Fluid flow and solute diffusion can be described by a combination of the continuity equation:

$$\mathrm{d}\rho/\mathrm{d}t = \rho\nabla\cdot\mathbf{v}, \tag{1}$$

the linear momentum conservation equation:

$$\mathrm{d}\mathbf{v}/\mathrm{d}t = 1/\rho\nabla P + \mu/\rho\nabla^2\mathbf{v} + 1/\rho\mathbf{F}^{\mathrm{ext}} \tag{2}$$

and the diffusion equation

$$\mathrm{d}C/\mathrm{d}t = D\nabla^2 C, \tag{3}$$

where $\mathbf{v}$ is the fluid velocity, $P$ is the fluid pressure, $\mathbf{F}^{\text{ext}}$ represents the effects of body forces (such as gravity acting on the fluid density), $\mu$ is the fluid viscosity, $\rho$ is the fluid density, $C$ is the concentration of a solute dissolved in the fluid (the concentration is defined as the mass dissolved in a unit volume of fluid) and $D$ is the molecular diffusion coefficient of the solute in the solvent.

For simplicity it is assumed that precipitation/dissolution processes can be described by a first-order kinetics reaction model:

$$D\nabla C \cdot \mathbf{n} = k(C_s - C_{eq}) \tag{4}$$

at the fluid–solid surface [19]. In the boundary condition (4), $\mathbf{n}$ is the unit vector in the direction normal to the interface pointing toward the fluid, $C_s$ is the solute concentration at the interface, $C_{eq}$ is the solute concentration in equilibrium with the solid and $k$ is the local reaction rate constant. If the solute is sufficiently dilute, the normal velocity, $\mathbf{v}_n$, at which the solid surface advances at position $\mathbf{x}_s$ on the fluid–solid interface into the liquid is given by

$$\mathbf{v}_n(\mathbf{x}_s) = D\nabla C(\mathbf{x}_s) \cdot \mathbf{n}/\rho_s, \tag{5}$$

where $\rho_s$ is the density of the precipitated solid phase. The interface condition in Eq. (5) relates the growth velocity to the diffusive flux of solute in the solution at the interface.

In the SPH simulations, both mobile fluids and solid boundaries are represented by particles. SPH simulations are based on the idea that continuous fields can be approximated by a linear (additive) superposition of smooth bell-shaped functions centered on point particles. Each particle is endowed with a set of extensive variables, $\{a\}$, and the corresponding scalar field, $A(\mathbf{r})$ is approximated by

$$A_S(\mathbf{r}) = \sum_i \frac{a_i}{n_i} W(\mathbf{r} - \mathbf{r}_i), \tag{6}$$

where $\mathbf{r}_i$ is the position of particle $i$, $n_i = \rho_i/m_i$ is the number density of particle $i$, $\rho_i$ and $m_i$ are the fluid density and mass of particle $i$ and $W$ is the SPH smoothing function. Similarly, the gradient of the scalar field $A$ is approximated by

$$\nabla A_S(\mathbf{r}) = \sum_i \frac{a_i}{n_i} \nabla_{\mathbf{r}} W(\mathbf{r} - \mathbf{r}_i). \tag{7}$$

The SPH approximations for continuous fields and their gradients (Eqs. (6) and (7)) allow the mass and momentum conservation equations for each particle to be written in the form [17]

$$n_i = \sum_j W(\mathbf{r}_j - \mathbf{r}_i) \quad i, j \in \text{fluid} + \text{solid particles} \tag{8}$$

and

$$\frac{d\mathbf{v}_i}{dt} = -\frac{1}{m_i} \sum_{j \in \text{fluid}+\text{solid}} \left( \frac{P_j}{n_j^2} + \frac{P_i}{n_i^2} \right) \nabla_i W(\mathbf{r}_i - \mathbf{r}_j) + \frac{1}{m_i} \sum_{j \in \text{fluid}+\text{solid}} \frac{(\mu_i + \mu_j)(\mathbf{v}_i - \mathbf{v}_j)}{n_i n_j (\mathbf{r}_i - \mathbf{r}_j)^2} (\mathbf{r}_i - \mathbf{r}_j) \cdot \nabla_i W(\mathbf{r}_i - \mathbf{r}_j, h) + \mathbf{F}_i^{\text{ext}} \quad i \in \text{fluid particles}. \tag{9}$$

Particles representing solids are frozen in space, but they enter into the calculation of forces acting on the fluid particles (Eq. (9)). The velocities of the particles representing solid-filled regions are set to zero, and the number density of the fluid at the particle locations is found from Eq. (8). Tartakovsky and Meakin [12] demonstrated that a combination of stationary "solid" particles with a bounce-back boundary condition (which returns fluid particles that penetrate into the solid domain to the fluid domain with reversed velocities) can be used to implement no-slip no-flow boundary conditions almost as accurately as the more rigorous but more complicated boundary condition proposed by Morris et al. [13] for which artificial velocities are assigned to the boundary particles. The bounce back boundary condition leads to velocity fields that deviate more from analytical results than the velocity fields obtained with the artificial velocity method [12]. On the other hand, the simplicity of the implementation and the computational efficiency of the bounce back boundary condition justify its use in more complex models.

To model reactive transport, the sink/source term is included in the SPH diffusion equation [15–17]:

$$\frac{\mathrm{d}C_i}{\mathrm{d}t} = \sum_{j\in\text{fluid}} \frac{(D_i n_i + D_j n_j)(C_i - C_j)}{n_i n_j (\mathbf{r}_i - \mathbf{r}_j)^2} (\mathbf{r}_i - \mathbf{r}_j)\cdot\nabla_i W(\mathbf{r}_i - \mathbf{r}_j, h) - R\sum_{k\in\text{solid}} (C_i - C_{\text{eq}})\delta_{ik}, \tag{10}$$

where $C_i$ is the solute concentration at fluid particle $i$, $R$ is the effective "particle" fluid–solid reaction rate constant, $\sum_{j\in\text{fluid}}$ indicates summation over all the fluid particles, $\sum_{k\in\text{solid}}$ indicates summation over all the solid particles and

$$\delta_{ik} = \begin{cases} 1, & |\mathbf{r}_i - \mathbf{r}_k| \leqslant d \\ 0, & |\mathbf{r}_i - \mathbf{r}_k| > d. \end{cases} \tag{11}$$

The solute concentration $C_i$ in Eq. (10) is defined in terms of the mass fraction of the solute, $C_i^*$ (the mass of solute dissolved in particle $i$ divided by the mass of solution carried by particle $i$), $C_i = C^*_{im_i n_{\text{eq}}}$, so the mass of the solute dissolved in particle $i$ is $C_i/n_{\text{eq}}$ where $n_{\text{eq}}$ is the equilibrium particle density (the equilibrium density of the particles).

The last term in Eq. (10) is the source term modeling the precipitation or dissolution reaction. The function $\delta_{ij}$ in the source term ensures that the precipitation/dissolution reaction occurs only in a thin layer of thickness $d$ near the fluid–solid interface. In reality, reactions between minerals and fluids take place in a thin zone with a width on the order of 1 nm at the fluid–solid interface. This width is much smaller than the range, $h$, of the SPH smoothing function, and the SPH approximation broadens the width of the fluid–solid interface to a value on the order of $h$.

The masses and viscosities of the fluid particles in Eq. (9) depend on the solute concentration. When the solute concentration is high, the concentration dependence of the solution density and viscosity can significantly affect the flow and result in flow instabilities such as viscous fingering, but in many subsurface applications concentrations are very low and fluid densities and viscosities can be treated as constants. In our previous work [17], a linear dependence of the particle masses and densities on solute concentration was assumed, and Eqs. (9) and (10) were used to simulate the Rayleigh–Taylor instability resulting from the gravity driven displacement of fresh water by salt water. In the subsurface, the concentrations of dissolved species are very low and in the present work it was assumed, for simplicity, that the masses and densities of the fluid particles are constant.

## 3. Precipitation and dissolution

The rate of gain/loss of mass due to precipitation/dissolution of the solid phase must balance the loss/gain of solute in the liquid phase. From Eq. (10), the rate of mass gain/loss due to interaction between fluid particle $i$ and solid particle $j$ is $-R_i(C_i - C_{\text{eq}})\delta_{ij}/n_{\text{eq}}$, and the rate of the mass gain/loss due to solid particle–fluid particle interaction is $R_i(C_i - C_{\text{eq}})\delta_{ij}/n_{\text{eq}}$. The total change of mass of solid particle $i$ due to interactions with all the fluid particles within distance $d$ is given by

$$\frac{\mathrm{d}m_i}{\mathrm{d}t} = \frac{R}{n_{\text{eq}}}\sum_{j\in\text{fluid}} (C_j - C_{\text{eq}})\delta_{ij} \quad i \in \text{solid}. \tag{12}$$

Since the "reaction interactions" between fluid–solid particles are anti-symmetric, the SPH reactive transport and precipitation model described by Eqs. (10) and (12) conserves the mass of the solute exactly. The processes of precipitation and dissolution are modeled by tracking the masses, $m_i$, of the solid particles. Once the mass of a solid particle $i$, $m_i$, reaches twice the original mass, $m_0$, the nearest fluid particle 'precipitates', becoming a new solid particle, the mass of the new solid particle is set to $m_0$ and the mass of the old solid particle becomes $m_i - m_0$. A similar approach for simulating surface growth has been used before in LB model simulations [19].

Similarly, if the mass of a solid particle reaches zero, the solid particle becomes a new fluid particle. Since the new fluid particles will be very close to the solid boundary, where the fluid velocity is very small, the initial velocity of a new fluid particle is set to zero.

The solid particles are added or removed due to precipitation and dissolution and the volumetric change in the fluid phase is exactly opposite to the volumetric change in the solid phase. The total change of the solid mass is described by Eq. (12). Because the volume of fluid changes so does the total mass of the solution. The

SPH model assumes that the change in the mass of the solution as a result of precipitation (the number of fluid particles decreases since $M$ fluid particles are replaced by the $M$ solid particles) is equal to the mass of solvent removed ($m_0 M$) plus the mass of the solute dissolved in the fluid particles replaced by the solid particles.

### 3.1. Relationship between k and R

The relationship between $k$ and $R$ can be found by comparing the fluxes given by Eqs. (4) and (5) and estimated from expression (12). The latter expression can be written in the approximate form:

$$\frac{\mathrm{d}\langle V\rangle}{\mathrm{d}t} \approx \frac{R}{\rho_s}\frac{N^{\mathrm{int}}}{n_{\mathrm{eq}}}(\langle C\rangle - C_{\mathrm{eq}}), \tag{13}$$

where $\langle V\rangle$ is the average volume of solid in a solid particle within distance $d$ from the interface, $\langle C\rangle$ is the average solute concentration carried by the fluid particle within distance $d$ from the fluid/solid interface and $N^{\mathrm{int}}$ is the average number of the fluid particles that interact with each solid particle. The approximate number of solid particles in a volume with unit fluid/solid interfacial area is $dh^{\mathscr{D}-1}n_{\mathrm{eq}}$ ($\mathscr{D}$ is the dimensionality of the system) and the total rate of growth of the solid volume per unit area, or normal velocity of the surface, $dn_{\mathrm{eq}}\frac{\mathrm{d}\langle V\rangle}{\mathrm{d}t} \approx \mathbf{v}_{\mathrm{n}}$ is given by

$$\mathbf{v}_{\mathrm{n}} \approx \frac{Rd}{\rho_s}N^{\mathrm{int}}(\langle C\rangle - C_{\mathrm{eq}}). \tag{14}$$

Comparing (14) with boundary conditions (4) and (5) for the diffusion equation yields the relationship

$$k \approx RdN^{\mathrm{int}} \tag{15}$$

between $k$ and $R$, where $N^{\mathrm{int}}$ depends on the particle number density, $d$, and, in general, the particle radial distribution function, $g(r)$. For particles placed on a two-dimensional square lattice, the average number of the fluid particles that interact with each solid particle, $N^{\mathrm{int}}$, can be easy calculated. For example for $n_{\mathrm{eq}} = 16$, $N^{\mathrm{int}}(d = 0.25) = 1$, $N^{\mathrm{int}}(d = 0.5) = 2.5$ and $N^{\mathrm{int}}(d = 1) = 10$ and from (15) $k(d = 0.25) = 0.25R$, $k(d = 0.5) = 1.25R$ and $k(d = 1) = 10R$. Numerical simulations presented in this paper show that these relationships between $k$ and $R$ also hold for irregularly distributed particles as long as the particle density for each particle (Eq. (8)) does not deviate significantly from the equilibrium particle density.

### 3.2. Instability of the precipitate front growth

Physically, the growth of a precipitate is an unstable process, and surface roughening will occur as a result of amplification of perturbations generated by small fluctuations (noise) in the growth process. The concentration gradient at a perturbation protruding into the liquid is larger than the average concentration gradient at the surface (and the concentration gradients at lagging parts of the front are smaller). Consequently the roughness of the interface grows because the most advanced parts of the interface (those more exposed to the supersaturated solution) grow faster than the lagging parts. The surface tension, which can be related to the thickness of the reactive layer, $d$, has a stabilizing effect on the surface growth. The early stages of surface roughening under diffusion-limited growth conditions are described by the Mullins–Sekerka linear stability analysis [20,21]. Mullins and Sekerka showed that for a sinusoidal perturbation with a wavelength of $\lambda$ or wavenumber of $k_\lambda = 2\pi/\lambda$ the growth velocity is given by

$$v(k_\lambda) = v_0 k_\lambda\left(1 - B\zeta_{\mathrm{C}}\zeta_{\mathrm{D}}k_\lambda^2\right) = v_0 W(k_\lambda), \tag{16}$$

where $\zeta_{\mathrm{D}}$ is the diffusion length, $\zeta_{\mathrm{C}}$ is the capillary length, $v_0$ is the average growth velocity and $B$ is a constant of order unity. The diffusion length is given by $\zeta_{\mathrm{D}} = D/v_0$, and the capillary length is given by $\zeta_{\mathrm{C}} = C_{\mathrm{eq}}\Gamma V_{\mathrm{m}}/\Delta CRT$, where $\Gamma$ is the interfacial energy, $R$ is the ideal gas constant, $V_{\mathrm{m}}$ is the molar volume in the solid phase and $\Delta C = C_\infty - C_{\mathrm{eq}}$, where $C_\infty$ is the far-field solute concentration. In the absence of an interfacial energy, $\zeta_{\mathrm{C}}$ is zero, and in accord with Eq. (16) the growth rate of the perturbation increases linearly with increasing wavenumber, $k_\lambda$. The effect of increasing the "reaction length", $d$, is to smoothen the growth rates over a length scale of order $d$. This cuts off the high wavenumber part of the dispersion function, $W(k_\lambda)$, leading to an effective dispersion

function that is very similar the dispersion function given in Eq. (16) with a non-zero capillary length. Consequently, the parameter $d$ plays the role of a non-zero capillary length or non-zero wavenumber cuttoff.

Besides surface tension, the stability of precipitate growth depends on the diffusion length, which can be related to the Damkohler number $Da = kL/D$, where $L$ is the characteristic size of the flow domain. Since the growth velocity increases with the velocity rate constant, $k$, a larger Damkohler number indicates a smaller diffusion length if the length $L$ is held constant.

## 4. SPH algorithm

At each time step in a simulation, the particle number density, $n_i$, is calculated using Eq. (8) and the pressure, $P_i$, is obtained using the equation of state

$$P_i = P_{\text{eq}} n_i / n_{\text{eq}} \tag{17}$$

for all particles $i$, where $P_{\text{eq}}$ is the equilibrium fluid pressure.

The particles acceleration, $\mathbf{a}_i = \mathrm{d}\mathbf{v}_i/\mathrm{d}t$, and the change of rate of concentration of each particle, $\mathrm{d}C_i/\mathrm{d}t$, is found from Eqs. (9) and (10) respectively. New fluid particle velocities, positions and concentrations are found by time integration using the explicit "velocity Verlet" algorithm [22], which takes the form

$$r_i(t+\Delta t) = r_i(t) + \Delta t \mathbf{v}_i(t) + 0.5\Delta t^2 \mathbf{a}_i(t), \tag{18}$$

$$C_i(t+\Delta t) = \left[ C_i(t) + 0.5\Delta t \left\{ \frac{\mathrm{d}C_i(t)}{\mathrm{d}t} + \frac{\mathrm{d}C_i(t+\Delta t)}{\mathrm{d}t} \right\} \right], \tag{19}$$

and

$$\mathbf{v}_i(t+\Delta t) = \mathbf{v}_i(t) + 0.5\Delta t \{ \mathbf{a}_i(t) + \mathbf{a}_i(t+\Delta t) \}. \tag{20}$$

The mass of the solid particles at time $t + \Delta t$ is given by

$$m_i(t+\Delta t) = m_i(t) + \frac{\Delta t}{2} \frac{R}{n_{\text{eq}}} \left\{ \sum_{j \in \text{fluid}} (C_j(t+\Delta t) - C_{\text{eq}}) \delta_{ij} + \sum_{j \in \text{fluid}} (C_j(t) - C_{\text{eq}}) \delta_{ij} \right\}, \qquad i \in \text{solid}. \tag{21}$$

To obtain a stable solution, the time step, $\Delta t$, must satisfy several conditions including the Courant–Friedrichs–Levy CFL condition [23]:

$$\Delta t \leqslant 0.25 h/3c, \tag{22}$$

a constraint due to the particle accelerations [24]:

$$\Delta t \leqslant 0.25 \min_i (h/3|\mathbf{a}_i|)^{1/2} \tag{23}$$

and a constraint due to viscous diffusion [13]:

$$\Delta t \leqslant \min_i (\rho_i h^2 / 9\mu_i), \tag{24}$$

where $c = \sqrt{P_{\text{eq}}/n_{\text{eq}}}$ is the sound velocity and $|\mathbf{a}_i|$ is the magnitude of the acceleration of particle $i$ [10].

A variety of forms, including spline functions $M_n$ with $(n-2)$ continuous derivatives proposed by Schoenberg [25] have been used for the smoothing functions. The $M_6$ smoothing function

$$W(\mathbf{r}, h) = \alpha \begin{cases} \left(3 - \frac{3|\mathbf{r}|}{h}\right)^5 - 6\left(2 - \frac{3|\mathbf{r}|}{h}\right)^5 + 15\left(1 - \frac{3|\mathbf{r}|}{h}\right)^5 & 0 \leqslant |\mathbf{r}| < h/3 \\ \left(3 - \frac{3|\mathbf{r}|}{h}\right)^5 - 6\left(2 - \frac{3|\mathbf{r}|}{h}\right)^5 & h/3 \leqslant |\mathbf{r}| < 2h/3 \\ \left(3 - \frac{3|\mathbf{r}|}{h}\right)^5 & 2h/3 \leqslant |\mathbf{r}| < h \\ 0 & h < |\mathbf{r}|, \end{cases} \tag{25}$$

where $\alpha = \frac{63}{478\pi h^2}$ and $\alpha = \frac{81}{359\pi h^3}$ in two and three spatial dimensions, was used in this work. The compact nature of the weighting function allows the number of particles required to calculate the density, change in linear momentum and change in concentration of particle $i$ to be reduced from the total number of particles to the number of particles located within a distance of $h$ from particle $i$. A linked-list approach with an underlying square lattice (for two-dimensional simulations) or cubic lattice (for three-dimensional simulations), with the size of the lattice unit equal to the range of the weighting function, $h$, for computational efficiency, was used to rapidly locate all of the particles within the range $h$ of the smoothing function from any selected particle. For computational convenience $h$ was set to unity.

## 5. Model validation

To validate the model, we conducted two-dimensional SPH simulations of a diffusion problem described by Eqs. (3)–(5) in an $L$ by $M$ (in units of $h$) rectangular domain ($0 < x < L$, with $L = 32$ and $0 < y < M$, with $M = 4$) filled with particles with an equilibrium particle density of $n_{eq} = 16$. A reaction boundary condition (4) was imposed at $x = 1$, a constant concentration was imposed at $x = L - 1$ ($C(x = L - 1, y) = C_0$), and periodic boundary conditions were used in the $y$ direction ($C(x, y = 0) = C(x, y = 4)$, $\partial C/\partial y|_{y=0} = \partial C/\partial y|_{y=4}$). The initial condition was $C(t = 0) = C_0 = 16$ and the equilibrium density was $C_{eq} = 2$. Particles with coordinates $(x < 1, y)$ were labeled as immobile solid boundary particles. The constant concentration at $x = L - 1$ was imposed by setting the solute concentration at the particles with coordinates $(x > L - 1)$ to $C_0$. The numerical solutions were obtained for 'reaction distances' of $d = 0.25$, 0.5 and 1 (in units of $h$).

### 5.1. Solution of linear diffusion problem (fixed reactive surface)

First the accuracy of the SPH solution of the diffusion Eq. (3) subject to the boundary condition (4) (diffusion and reaction only) was verified. The density of the solid phase was assumed to be infinitely large resulting, based on Eq. (5), in an infinitesimally small solid surface velocity, so the reactive surface can be treated as a stationary solute sink. The analytical solution of the one-dimensional diffusion Eq. (3) subject to the boundary condition expressed in Eq. (4) at $x = 1$, the prescribed concentration boundary condition $C = C_0$ at $x = L'$ ($L' = L - 1$) and the initial condition $C = C_0$ is:

$$C(x,t) = \sum_{n=1}^{\infty} a_n e^{-\lambda_n^2 D t} \sin[\lambda_n (L' - x)] + \frac{k(C_0 - C_{eq})}{D - kL''}(L' - x) + C_0, \quad 1 \leqslant x \leqslant L', \tag{26}$$

where

$$a_m = \frac{k(C_0 - C_{eq})}{kL'' - D} \frac{2}{\lambda_m} \frac{[-\lambda_m L'' \cos \lambda_m L'' + \sin \lambda_m L'']}{\lambda_m L'' - \sin \lambda_m L'' \cos \lambda_m L''}. \tag{27}$$

In Eqs. (26) and (27), $\lambda_n$ is the solution of $D\lambda_n/k = \tan \lambda_n L''$ and $L'' = L - 2$.

The SPH solution was obtained with particles located on a regular lattice and positioned irregularly but with uniform density ($n_i \approx n_{eq}$ for all $i$). It is useful to investigate the effect of particle disorder on the accuracy of the SPH simulations, because in simulations of fluid flow the configuration of the SPH particles representing the fluid will unavoidably change and become disordered, even if the original particle configuration was perfectly ordered. However, the particles do not become "completely" disordered in the sense that the fluctuations in the particle densities $n_i$ are limited by fluid compressibility and controlled by the equation of state (17). In the absence of external forces, $\mathbf{F}^{ext} = 0$ in Eq. (9), the particles would be in a stationary disordered state. To study the effect of equilibrium particle disorder, particles were randomly inserted into a $32 \times 16$ box (in units of $h$). Then Eq. (9) with $\mathbf{F}^{ext} = 0$ and periodic flow boundary conditions was applied to the particle system until it reached an almost uniform equilibrium state (fluctuations in the densities measured at the particle centers via Eq. (1) or Eq. (8) were smaller than 0.001%). This eliminates long range density fluctuations and leaves the system in a locally disordered state.

We found that the SPH solution obtained with both regular and irregular particle distributions compares very well with the analytical solution for all values of $d$. Fig. 1 shows the concentration as a function of $x$ at

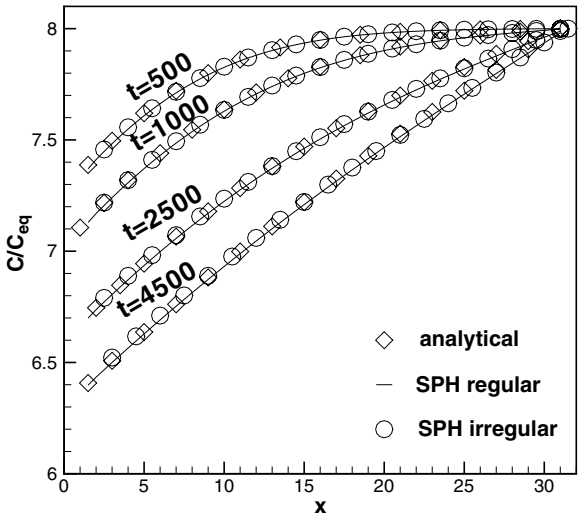


Fig. 1. Dimensionless concentration $C/C_{eq}$ versus distance (in units of $h$) at different times (in dimensionless SPH model time units) obtained analytically (open diamonds) and from SPH simulations with regular (solid line) and irregular (open circles) particle placement with $d = 0.25$ (in units of $h$), $L = 32$ (in units of $h$), $Da = 0.375$, $k/R = 0.25$ (in units of $h$), $C_0/C_{eq} = 8$ ($D = 0.1$, $R = 0.005$, $k = 0.00125$).

different times obtained analytically from expression (26) and from SPH simulations with $D = 0.1$, $k = 0.00125$, $C_0/C_{eq} = 8$ and $d = 0.25$. Fig. 2 shows similar results for $d = 0.5$. Figs. 1 and 2 show very good agreement between the analytical and SPH solutions obtained with both regular and irregular particle placement.

### 5.2. Solution of a non-linear diffusion problem (moving reactive surface)

Next we verified the accuracy of the SPH solution of the non-linear diffusion problem with a moving liquid–solid interface given by Eq. (5). For simplicity, the density of the solid phase was made equal to the density of fluid, so that the initial mass of the solid particles, $m_0$, was equal to unity.

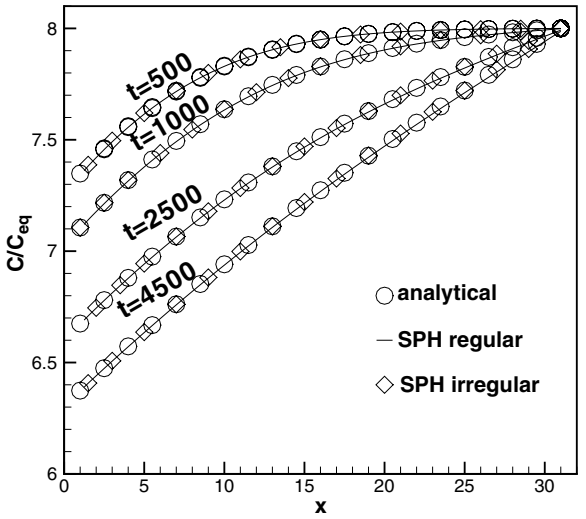


Fig. 2. Dimensionless concentration $C/C_{eq}$ versus distance (in units of $h$) at different times (in dimensionless SPH model time units) obtained analytically (open circles) and with SPH with regular (solid line) and irregular (open diamonds) particle placement with $d = 0.5$ (in units of $h$), $L = 32$ (in units of $h$), $Da = 0.375$, $k/R = 1.25$ (in units of $h$), $C_0/C_{eq} = 8$ ($D = 0.1$, $R = 0.001$, $k = 0.00125$).

If noise (or random numerical errors) can be avoided and the initial solid boundary is perfectly flat (this can be achieved only by placing SPH particles on a regular lattice) the growing surface will remain flat. Under these conditions, the problem of diffusion and boundary growth in the domain described above is governed by the one-dimensional diffusion Eq. (3) subject to the one-dimensional versions of boundary conditions (4) and (5) at $x = L'$, a prescribed concentration boundary condition at $x = 1$ ($C(x = 1,y) = C_0$), the initial concentration distribution $C(t = 0) = C_0$ and the initial position of the solid boundary $S$, $S(t = 0) = S_0$, where $S_0 = L'$. Analytical solution of this non-linear problem is complicated by the moving boundary. To simplify the derivation of an analytical solution it is commonly assumed [26] that for slow growth processes with small Peclet numbers the time derivative in the diffusion equation can be disregarded (a quasi-stationary approximation is used). Under this assumption, the analytical solution of this problem is

$$S(t) = (D/k + L') - \sqrt{(D/k + L' - S_0)^2 - 2D(C_0 - C_{eq})t/\rho_m}. \tag{28}$$

The SPH precipitation model may result in an artificially increased average precipitate density depending on the value chosen for $d$. For large $d$ not all solid particles reacting with the fluid particles have time to double their masses before the fluid–solid front advances sufficiently for these particles to become non-reactive with masses greater than $m_0$. In the simulations with $d = 0.25$, the average density of the solid particles in the precipitate, $\rho_m$, is $m_0 n_{eq}$, for $d = 0.5$ $\rho_m = 1.25 m_0 n_{eq}$, and for $d = 1$ $\rho_m = 1.47 m_0 n_{eq}$.

Figs. 3–5 show the front position as a function of time obtained analytically and from SPH simulations with $d = 0.25$, 0.5 and 1, respectively. The parameters $D = 1$, $k = 0.001$ and $C_0/C_{eq} = 8$ were used in these simulations. The SPH solution for uniform front growth (obtained with regular particle placement) compares very well with the analytical solution (28) for $d = 0.25$ (Fig. 3) and $d = 0.5$ (Fig. 4). For $d = 1$, the SPH solution fluctuates slightly around the analytical solution, see Fig. 5. SPH simulations with irregular particle distributions introduce random noise at the surface, and this leads to non-uniform surface growth. Figs. 6–8 show unstable growth of the interface, initially perturbed as a result of irregularly particle placement, for $d = 0.25$, 0.5 and 1, respectively. The roughness of the front decreases with increasing $d$. Fig. 9 depicts the variance of the front, the mean square deviation of the front position from the average position of the rough front, as a function of the average front position for differenet values of $d$. Fig. 9 shows that the front variance increases with average front position and decreases with increasing $d$. It can be seen that an increase in $d$ produces a smoother front, indicating that $d$ acts as a surface tension and has a stabilizing effect on the surface growth. Figs. 3–5 also compare the time dependence of the average position of the front calculated with non-uniformly placed particles with the time dependent front positions calculated analytically and using regularly

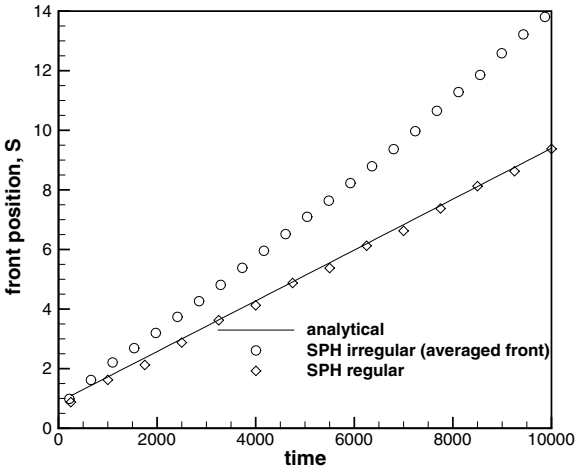


Fig. 3. Position of the solid boundaries (in units of $h$) as a function of time (in dimensionless SPH model time units) obtained from SPH simulations with irregular (open circles) and regular (open diamonds) particle placements and the analytical solution (solid line) of the diffusion equation with a moving boundary. $d = 0.25$ (in units of $h$), $L = 32$ (in units of $h$), $Da = 0.03$, $k/R = 0.25$ (in units of $h$), $C_0/C_{eq} = 8$, $\rho_m = m_0 n_{eq}$ ($D = 1$, $R = 0.004$, $k = 0.001$).

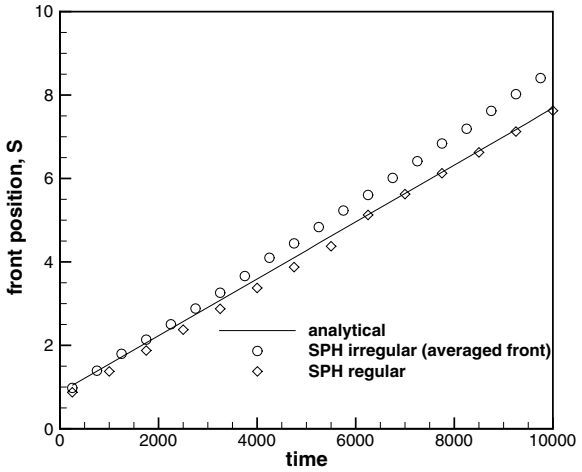


Fig. 4. Position of the solid boundaries (in units of $h$) as a function of time (in dimensionless SPH model time units) obtained from SPH simulations with irregular (open circles) and regular (open diamonds) particle placements and the analytical solution of the diffusion equation with moving boundary (solid line). $d = 0.5$ (in units of $h$), $L = 32$ (in units of $h$), $Da = 0.03$, $k/R = 1.25$ (in units of $h$), $C_0/C_{eq} = 8$, $\rho_m = 1.25 m_0 n_{eq}$ ($D = 0.1$, $R = 0.0008$, $k = 0.001$).

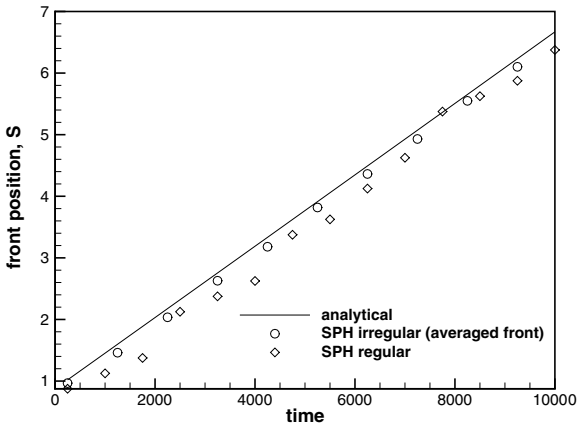


Fig. 5. Position of the solid boundaries (in units of $h$) as a function of time (in dimensionless SPH model time units) obtained from SPH simulations with irregular (open circles) and regular (open diamonds) particle placements and the analytical solution (solid line) of the diffusion equation with a moving boundary. $d = 1$ (in units of $h$), $L = 32$ (in units of $h$), $Da = 0.03$, $k/R = 10$ (in units of $h$), $C_0/C_{eq} = 8$, $\rho_m = 1.47 m_0 n_{eq}$ ($D = 1$, $R = 0.0001$, $k = 0.001$).

placed particles. The average positions of the non-uniform fronts obtained with $d = 0.25$ and $d = 0.5$ propagate faster than the uniform front. The rate of propagation of the non-uniform front increases with decreasing $d$ and with time as the front becomes more irregular. On the other hand, the average position of the more stable front obtained with $d = 1$ advances with the same rate as the uniform front. A two-fold increase in resolution (from $L/h = 32$ to $L/h = 64$) increased the average front position by less than 2%.

### 5.3. Precipitation in the presence of flow

To further investigate the effect of particle disorder, precipitation in the presence of fluid flow was investigated. The flow was initiated by applying uniform body forces acting on the particle masses in the $y$ direction. The particles with $x$ coordinates greater than 31 were prescribed a constant concentration of $C = C_0$, and they were frozen in space to created a no-flow boundary condition for the Navier–Stokes equation (the solid reac-

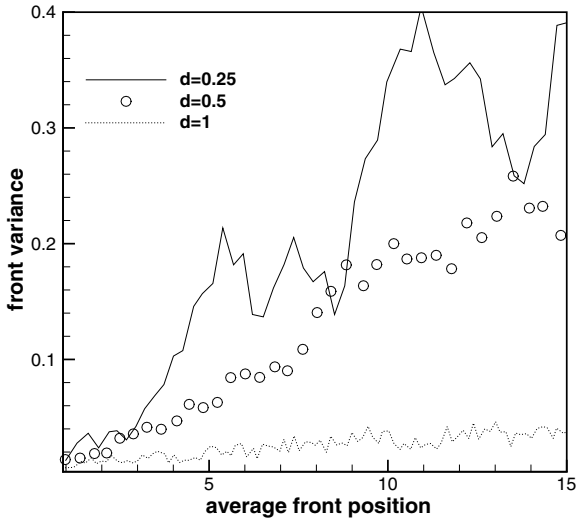


Fig. 9. The front variances as a function of average front position for non-uniform surface growth, with $d = 0.25$, 0.5 and 1, shown in Figs. 6–8.

tive surface initially located at $x = 1$ also served as a no-flow boundary). The initial concentration of the fluid particles was assigned a value of $C_0$, and periodic boundary conditions were imposed at the vertical boundaries. Apart from the small disturbances at the perturbed solid boundaries, the concentration profile and precipitation rate should not be affected by the flow. The average position of the front as a function of time for this simulation is shown in Fig. 10. It can be seen that at early times in the simulations, the perturbed front grows with the same velocity as the unperturbed front. It shows that particle disorder caused by the laminar flow does not significantly affect the accuracy of the SPH solution of the diffusion equation and the SPH precipitation (adsorption) model. The initial Reynolds number was $Re = 864$ and the Peclet number was $Pe = 54$, both of which decreased with time as the gap between the upper and lower no-flow boundaries decreased as a result of precipitation. At later times, the precipitation front propagation rate in the presence of fluid flow was slightly larger than the front propagation rate in the absence of flow. While a small increase in the front propagation velocity could be a result of increasing particle disorder with increasing time, it could be also a result

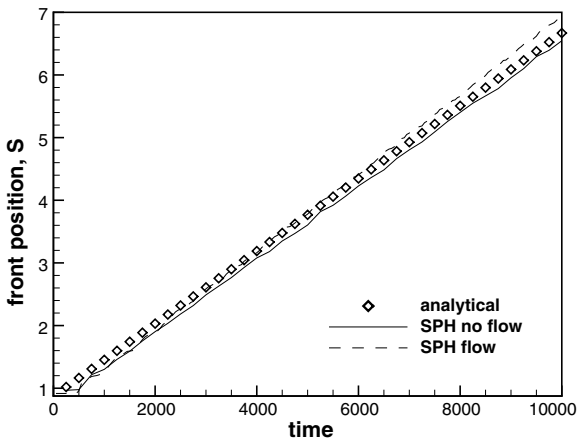


Fig. 10. Position of the solid boundaries as a function of time (in dimensionless SPH model time units) obtained from SPH simulations in the absence of fluid flow (solid line) and in the presence of flow (broken line) and the analytical solution (open diamonds) of the diffusion equation with a moving boundary. $Da = 0.03$, $d = 1$. In the flow simulations, the Reynolds number was $Re = 864$ and the Peclet number was $Pe = 54$.

of the slight increase in solute concentration at the solid boundary due to the fluid mixing caused by the growth of front perturbations. In addition, fluid flow parallel to a rough surface could bring more concentrated solution into proximity with the protruding parts of the surface leading to faster growth of the protrusions and more unstable surface growth (more rapid growth of the surface roughness).

The error due to particle disorder can be significantly reduced by periodically remeshing the particles [18,27].

### 5.4. Effect of Damkohler number and reaction length parameter d on the nucleus growth

First we studied the effect of the Damkohler number on the growth of an initially perturbed circle (with a radius given by $r = 10 + 5\cos(4\theta)$, $0 < \theta < 2\pi$). The initial solute concentration was set to $8C_{eq}$, a constant concentration of $8C_{eq}$ was maintained at a distance $L = 30$ from the center of perturbed circle, and the boundary conditions given in Eqs. (4) and (5) were imposed at the surface of the perturbed circle. The reaction length parameter $d$ was set to $d = 0.5$. Growth with $Da = 37.5$ ($R = 1$, $k = 1.25$, $D = 1$) produced a highly unstable dendritic structure (Fig. 11a) while growth with $Da = 3.75$ ($R = 0.1$, $k = 0.125$, $D = 1$) resulted in the formation of a more compact and regular (almost symmetric) morphology (Fig. 11b). This is also consistent with the Mullins–Sekerka Eq. (16). The diffusion length in the simulation used to obtain Fig. 11a is smaller than the diffusion length in the simulation used to obtain Fig. 11b, and a longer diffusion length is expected to lead to a more stable growth process (a process in which instabilities grow more slowly and the minimum unstable wavelength is longer).

Figs. 12 and 13 show the effect of the Damkohler number, $Da$, on growth from a small circular nucleus with a radius of 0.5 (in units of $h$) located in the center of the computational domain. A constant concentration of $C_0 = 16$ was maintained at a distance of $L = 64$ (in units of $h$) from the center of the nucleus. The equilibrium concentration, $C_{eq}$, was set to 13.3. Table 1 gives a summary of parameters used in these simulations, and the effective fractal dimension, $D_f$, of the resulting precipitating structures. The effective fractal dimension, $D_f$, was found from the relationship:

$$N_{part} \sim r^{D_f}, \tag{29}$$

where $N_{part}$ is the number of solid particles within the distance $r$ from the center of the nucleus. For an ideal fractal, Eq. (29) describes the mass/length scaling over an infinite range of length scales [28]. For finite objects with characteristic lengths (such as the particle size, the nucleus size and the radius of the pattern for the morphologies shown in Fig. 12) this relationship holds approximately over the intervening length scales, and the exponent, $D_f$, obtained using Eq. (29) is called the effective fractal dimension. Fig. 13 shows, that for $r$ greater than several $h$ and smaller than 85% of the size of the pattern, $\ln(N_{part})$ increases linearly with $\ln(r)$ indicating

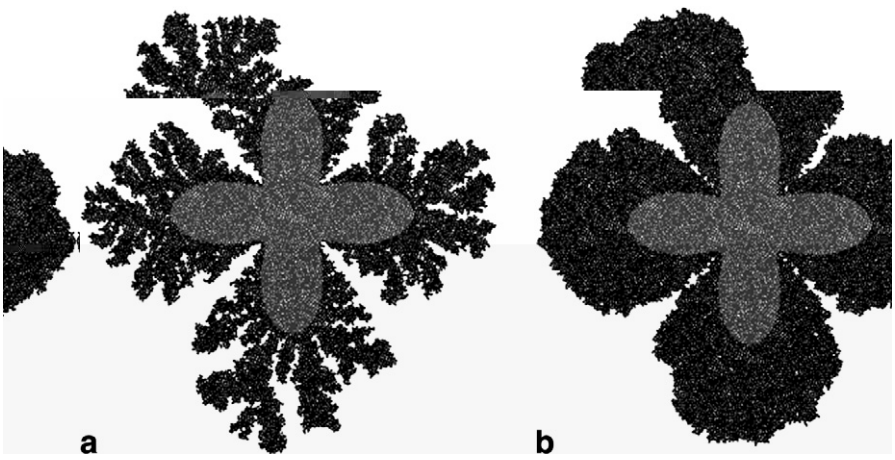


Fig. 11. Growth of perturbed circle with $d = 0.5$. (a) $Da = 37.5$; (b) $Da = 3.75$. Gray particles show the initial shape of the perturbed circle.

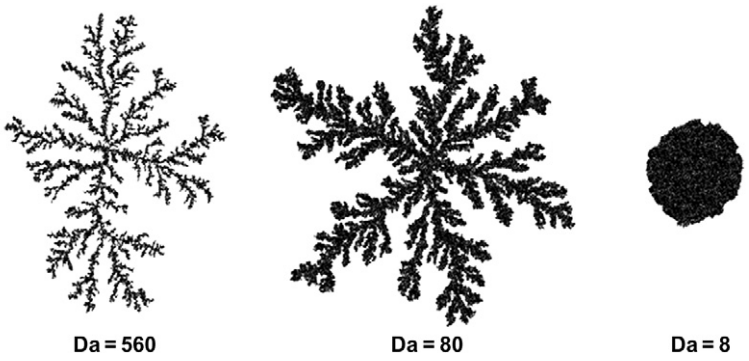


Fig. 12. Growth from the nucleus with $d = 0.5$ and $Da = 560$, 80 and 8.

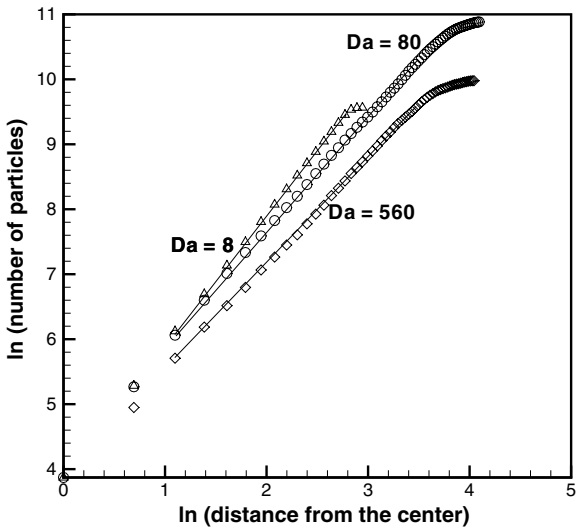


Fig. 13. Logarithm of the number of particles within the distance $r$ from the center of a nucleus versus the logarithm of $r$ for the simulations depicted in Fig. 11.

Table 1
Parameters of the simulations of the crystal growth from the nucleus

| $d$ | $R/k$ | $D$ | $Da = kL/D$ | Fractal dimension |
|---|---|---|---|---|
| 0.5 | 7/8.75 | 1 | 560 | 1.66 |
| 0.5 | 1/1.25 | 1 | 80 | 1.74 |
| 0.5 | 0.1/0.125 | 1 | 8 | 2 |
| 1.0 | 0.76/8.74 | 1 | 560 | 1.67 |

that the growing structures are fractals. For $Da = 560$ and $d = 0.5$ the growth results in a disorderly dendritic structure with an effective fractal dimension of $D_f = 1.66$. For the closely related diffusion limited aggregation (DLA) model [28,29] an effective fractal dimension of about 1.715 is obtained from off-lattice simulations [30] and a somewhat smaller fractal dimension is obtained from lattice models ($D_f \approx 1.68$ for large clusters on a square lattice [31]). The effective fractal dimension of 1.66 obtained for the pattern shown on the left-hand side of Fig. 12 (which covers a relatively small range of length scales) which was obtained using a Damkohler number of 560 is consistent with the idea that the SPH precipitation model in the $Da \to \infty$ limit is essentially equivalent to (is in the same universality class as) the DLA model. Because the constant concentration bound-

ary condition is not imposed at infinity ($Da \neq \infty$), the initial solute concentration is not zero and the concentration imposed at the distant boundary does approach the $C_O \to 0$ limit ($\zeta_D \neq \infty$), the growth process is not exactly a DLA process, and for this reason we expect that the branched pattern is not exactly a DLA fractal. This is another reason why $D_f$ is an effective fractal dimension. For $Da = 8$ and $d = 0.5$, the effective fractal dimension was $D_f = 2$ (the pattern is compact and uniformly fills the two-dimensional space). These results are also consistent with the Lattice Boltzmann crystal growth simulations of Kang et al. [19] who obtained $D_f = 2$ from their model with $Da = 2$ and $D_f = 1.75$ for growth with $Da = 600$. Discrepancies on the order of 0.1 in the effective fractal dimension are not surprising when the range of length scales between characteristic lengths is on the order of one to two decades, and the growth process is not in the asymptotic DLA limit. The effective fractal dimension depends on the method used to estimate the fractal dimension, the range of length scales and the cross-over/finite size effects, which can depend on model details.

We found that the increase in $d$ leads to a fractal dendritic pattern with thicker branches. Similar patterns are obtained with diffusion limited aggregation models with sticking probabilities less than unity (the randomly walking particles do not always stick the first time they contact the growing cluster) that increase as the coordination number of the unoccupied surface sites increase [30]. A similar effect results from including the effects of surface energy (the growth rate is enhanced in concave regions and diminished in convex regions) and the thickening of the branches is consistent with the idea that an increase in the reaction length, $d$, has an effect similar to increasing the surface energy.

## 6. Flow, reactive transport and precipitation in fractures

The full capabilities of the SPH model were illustrated by simulating flow, reactive transport and precipitation in a rough-walled three-dimensional fracture. A self-affine fractal model with a Hurst exponent of 0.7 was used to generate the geometry of the fracture walls. The fractal model is based on numerous observations indicating that the fracture surfaces of brittle materials, including rocks, have a self-affine fractal geometry, which can be characterized by a Hurst exponent with a more or less material independent (quasi-universal) value of about 0.7 [32]. The algorithm used to generate the fracture walls and the geometry of the fracture aperture is described in Tartakovsky and Meakin [17]. The fracture size in the lateral directions (parallel to the plane of the fracture) was $16 \times 16$ in units of $h$ and the (vertical) thickness of the computational domain was $16h$.

To set up an SPH simulation the particles were randomly placed in the $16 \times 16 \times 16$ domain and then equilibrated using the SPH equation of motion with zero gravitational acceleration. After the particle densities, $n_i$, became uniform, the fracture geometry was imposed on the particle system. The particles inside the fracture were designated as fluid particles, the particles outside of the fracture aperture, within a distance $h$ from the self-affine surfaces, were 'frozen' and labeled as boundary particles creating the fracture walls, and the rest of the particles were removed. Periodic flow boundary conditions were used in the $x$ and $y$ directions, parallel to the plane of the fracture. The flow was initiated by applying a gravitational acceleration of $g = 0.01$. The volume of the fracture aperture was $709h^3$, the equilibrium particle number density, $n_{eq}$, was 36, and the total number of mobile particles representing the fluid was 25,513. The equilibrium pressure, $P_{eq}$, was assigned a value of 144, and a viscosity of $\mu = 3$ was used.

Once the flow of the fluid representing the solvent had reached a steady state, the time was set to zero, $d$ was set to 1, the initial concentration of the solute in the fracture was set to $C_{eq} = 2$, and solute with a concentration of $C = 4C_{eq}$ was injected at $5 < x < 6$. The corresponding boundary condition $C(5 < x < 6) = 4C_{eq}$ was implemented by setting the concentrations $C_i$ of the particles $i$ that passed the injection zone to $4C_{eq}$. Fig. 14 shows a three-dimensional view of the minerals precipitated on the walls of the fracture (the upper wall of the fracture was removed for better visualization) and several cross-sections in the direction parallel to the flow at dimensionless time of $t = 520$. Precipitation (the precipitated mineral is denoted by red particles) occurs around the solute injection area. Fig. 15 shows the average fluid flux $q$ through a cross-section of the fracture perpendicular to the direction of flow, $q = \int_S v_x(\mathbf{x})d\mathbf{x}/S_A$ ($v_x$ is the $x$-component of the velocity vector, $S$ is the cross-section of the fracture aperture at $x = 16$ and $S_A$ is the cross-section area at the start of the simulation). The figure shows that the flow through the fracture aperture decreases as the aperture is occluded by the precipitated solid. In continuum subsurface reactive transport simulations it is common

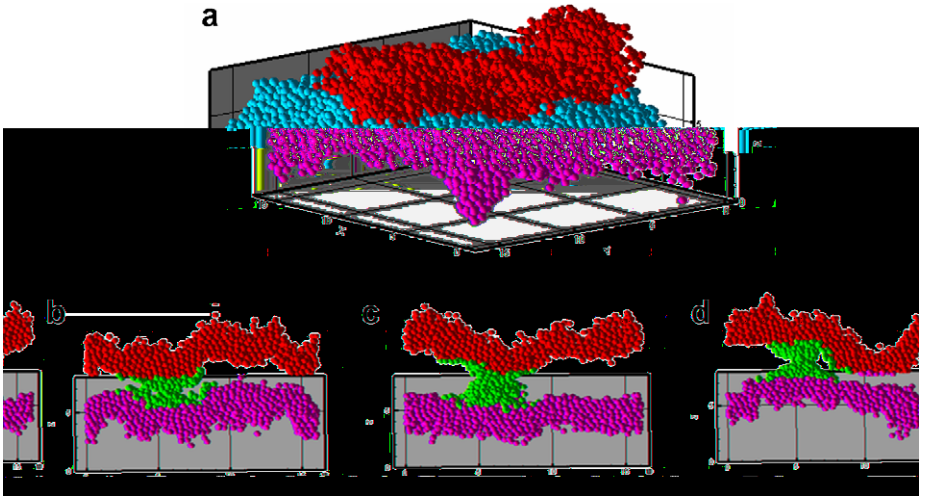


Fig. 14. Mineral precipitation in a fracture aperture with self-affine walls resulting from reactive transport with $Da' = 1.37$ and $Pe = 19.43$ at dimensionless time $t = 520$: (a) a three-dimensional view of the precipitated minerals (red particles) and lower fracture wall (light blue particles); (b–d) cross-sections in the direction parallel to the flow at $y = 4$, 8 and $12h$. The dark and light blue particles represent the upper and lower walls of the fracture (For interpretation of the references to color in this figure legend, the reader is referred to the web version of this article.).

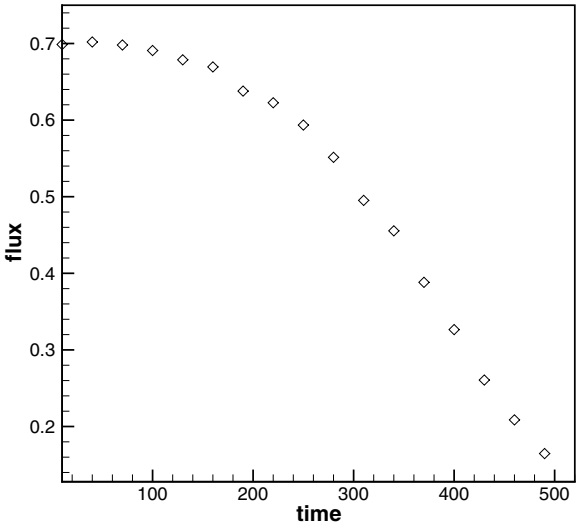


Fig. 15. Flux $q$ (in units of $h$ per dimensionless SPH model time unit), versus dimensionless SPH model time for reactive transport in the fracture shown in Fig. 9. $Da' = 1.37$ and $Pe = 19.43$.

[33] to describe the changes in the average concentration in the fractures $\langle C_f \rangle = \int_{V_r} C(\mathbf{x})d\mathbf{x}/V_r$ ($V_r$ is the representative volume of the fracture) using an effective reaction rate coefficient $R_{ef}$. The rate coefficient, $R_{ef}$, can be calculated from

$$\frac{\partial \langle C_f \rangle_r}{\partial t} = R_{ef}[\langle C_f \rangle - C_{eq}], \tag{30}$$

where $\partial \langle C_f \rangle_r / \partial t$ is the change in the average concentration due to reaction only. Fig. 16 shows the dependence of $\partial \langle C_f \rangle_r / \partial t$ on $\langle C_f \rangle - C_{eq}$ calculated during the reactive transport simulation. The slope is proportional to the

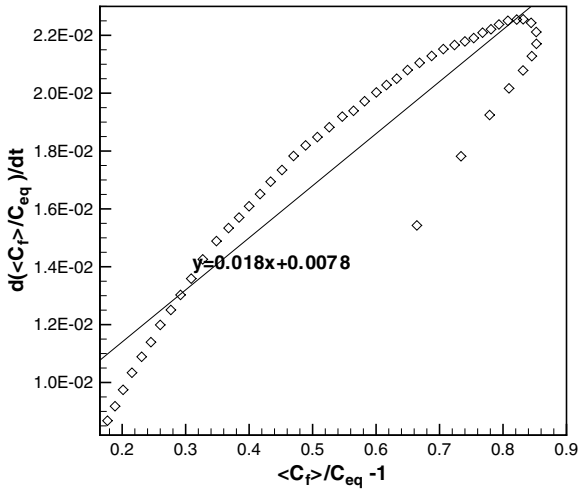


Fig. 16. Rate of change in dimensionless average concentration, $\langle C_f\rangle/C_{eq}$, due to reaction versus $\langle C\rangle/C_{eq} - 1$. $Da' = 1.37$ and $Pe = 19.43$. The solid line is the best linear fit to the data. The slope of the line is the effective reaction rate coefficient for the fracture.

effective rate constant, $R_{ef}$. It can be seen that $\partial\langle C_f\rangle_r/\partial t$, and hence $R_{ef}$, changes non-linearly during the simulation, and the dependence of $\partial\langle C_f\rangle_r/\partial t$ on $\langle C_f\rangle - C_{eq}$ has two branches resulting in non-constant and non-unique (multi-valued) reaction rate coefficients. The concentration in the fracture initially increases because of advection. Later on, advection decreases as precipitated minerals begin to occlude the fracture aperture and reduce the fluid flux, and the solute concentration in the aperture decreases because the flux of solute into the aperture decreases. The non-unique behavior of $R_{ef}$ during the early and later parts of the simulation may result from the changing reactive surface area of the fracture. The average effective rate coefficient can be found by fitting a straight line to the data in Fig. 16. For the simulation described above the value of the average effective reaction rate coefficient is $K_{ef} = 0.018$. The dimensionless numbers (the Damkohler and Peclet numbers) controlling reactive transport for this simulation are: $Da' = R_{ef}l^2/D = 1.37$ and $Pe = ql/D = 19.43$, where $l = 2.76$ (in units of $h$) is the average width of the fracture aperture and $q = 0.7$ is the average flux (both estimated before precipitation occurred). From Fig. 14 it can be seen that due to the relatively large Damkohler number precipitation occurred mainly around the solute injection region. As the Damkohler number decreases and/or the Peclet number increases precipitation along the fracture wall will become more uniform. A detailed study of the effects of the Damkochler and Peclet numbers on precipitation in three-dimensional fractured and porous media will be a subject of the future research.

## 7. Conclusions

A new numerical model for reactive transport and mineral precipitation in fractured and porous materials, based on SPH, was developed. The surface reaction, usually treated using a mixed boundary condition, is modeled through solid–fluid particles interactions added into the SPH diffusion Eq. (10). The unique relationship between the "particle" fluid–solid reaction rate constant, $R$, and the standard local reaction rate constant, $k$, was derived. The SPH solution of the diffusion equation was validated against analytical solutions for cases in which the surface growth can be disregarded (the linear diffusion problem) and for uniform surface growth (non-linear surface growth). It was found that initial perturbation of the solid surface caused by an irregular particle distribution leads to unstable growth. An increase in the reaction length parameter, $d$, was found to have a stabilizing effect on the non-uniform surface growth. Fluid flow along the reactive surface slightly increased the precipitation rate. The slight increase in the growth rate could be due to increased particle disorder but it could also be due to increased mixing and higher solute concentrations at the growing reactive surface.

The SPH model was used to simulate growth from a nucleus in a supersaturated solution, and it was found that this produces fractal structures with effective fractal dimensions ranging from $D_f = 2$ for compact growth

in the reaction-limited growth limit (small Da number) to $D_f = 1.66$ for the dendrite structures in the diffusion-limited growth limit (large Da number). The upper limit of the fractal dimension corresponds to the dimension of the embedding space. The lower limit is close to the fractal dimension ($D_f \approx 1.7$) found for diffusion controlled cluster formation. A similar relationship between the Damkohler number and the fractal dimension of the dendritic structure was found in Lattice Boltzmann growth simulations. An increase in the reaction length, $d$, resulted in a more compact growth with larger fractal dimension.

The SPH model was also used to simulate three-dimensional reactive transport in a fracture aperture with self-affine fractal surfaces. The results were used to calculate the effective reactive rate coefficient of the fracture. A non-unique time-dependent effective reaction rate coefficient was observed. The results illustrate that the SPH based reactive transport model can be successfully used to study complex coupled phenomena such flow, reactive transport and precipitation in porous and fractured media.

One of the deficiencies of the SPH, and other Lagrangian particle methods, is the high computational cost in comparison with the grid-based numerical methods. The three-dimensional simulations (consisting of 52,000 time steps with a 72,169 particle system) described in this paper required approximately 100 h of CPU time on a PC with a 3.0 GHz processor. Fortunately, SPH is similar to molecular dynamics methods. Consequently, SPH code that runs efficiently on parallel computers with a variety of architectures can be developed, and the growing speed of modern computers will make it possible to significantly increase the resolution of the simulations and reduce computational time in the near future.

## Acknowledgments

We acknowledge P. Koumoutsakos, and three anonymous referees for helpful remarks that helped us improve the manuscript. This research was supported by the Laboratory Directed Research and Development program and by the Multiscale Mathematics Research and Education program, Advanced Scientific Computing Research, US Department of Energy, Office of Science DE-AC06-76RLO 1830. Paul Meakin was partially supported by the Environmental Management Science Program of the Office of Science, US Department of Energy under contract DE-AC07-05ID14517. The Pacific Northwest National Laboratory is operated by the Battelle Memorial Institute and the Idaho National Laboratory is operated by the Battelle Energy Alliance.

## References

[1] Q. Kang, D. Zhang, S. Chen, Simulation of dissolution and precipitation in porous media, Journal of Geophysical Research 109 (2003) 2505.
[2] D. Zhang, Q. Kang, Pore scale simulation of solute transport in fractured porous media, Geophysical Research Letter 31 (2004) L125404.
[3] C.E. Knutson, C.J. Werth, A.J. Valocchi, Pore-scale simulations of biomass growth along the transverse mixing zone of a model two-dimensional porous medium, Water Resources Research 41 (2005) W07007.
[4] B. Bijeljic, M.J. Blunt, Pore-scale modeling and continuous time random walk analysis of dispersion in porous media, Water Resources Research 42 (2006) W01202.
[5] B. Bijeljic, A.H. Muggeridge, M.J. Blunt, Pore-sale modeling of longitudinal dispersion, Water Resources Research 40 (2004) W11501.
[6] L. de Arcangelis, J. Koplik, S. Redner, D. Wilkinson, Hydrodynamic dispersion in network models of porous-media, Physical Review Letters 57 (1986) 996–999.
[7] L.B. Lucy, Numerical approach to the testing of the fission hypothesis, Astronomical Journal 82 (1977) 1013.
[8] R.A. Gingold, J.J. Monaghan, Smoothed particle hydrodynamics: theory and application to non-spherical stars, Monthly Notices of the Royal Astronomical Society 181 (1977) 375.
[9] M.B. Liu, G.R. Liu, K.Y. Lam, Computer simulation of high explosive explosion using smoothed particle hydrodynamics methodology, Computers and Fluids 32 (2003) 305.
[10] J.J. Monaghan, Simulating free surface flows with SPH, Journal of Computational Physics 110 (1994) 399.
[11] A.M. Tartakovsky, P. Meakin, Modeling of surface tension and contact angles with smoothed particle hydrodynamics, Physical Review E72 (2005) 026301.
[12] A.M. Tartakovsky, P. Meakin, Simulation of free-surface flow and injection of fluids into fracture apertures using smoothed particle hydrodynamics, Vadose Zone Journal 4 (2005) 848.
[13] J.P. Morris, P.J. Fox, Y. Zhu, Modeling low Reynolds number incompressible flows using SPH, Journal of Computational Physics 136 (1997) 214.

[14] Y. Zhu, P.J. Fox, J.P. Morris, A pore-scale numerical model for flow through porous media, International Journal for Numerical and Analytical Methods in Geomechanics 23 (1999) 881.
[15] Y. Zhu, P.J. Fox, Smoothed particle hydrodynamics model for diffusion through porous media, Transport in Porous Media 43 (2001) 441.
[16] Y. Zhu, P.J. Fox, Simulation of pore-scale dispersion in periodic porous media using smoothed particle hydrodynamics, Journal of Computational Physics 182 (2002) 622.
[17] A.M. Tartakovsky, P. Meakin, A smoothed particle hydrodynamics model for miscible flow in three-dimensional fractures and the two-dimensional Rayleigh–Taylor instability, Journal Computational Physics 207 (2005) 610.
[18] A.K. Chaniotis, C.E. Frouzakis, J.C. Lee, A.G. Tomboulides, D. Poulikakos, K. Boulouchos, Remeshed smoothed particle hydrodynamics for the simulation of laminar chemically reactive flows, Journal of Computational Physics 191 (2003) 1–17.
[19] Q. Kang, D. Zhang, P. Lichtner, I. Tsimpanogiannis, Lattice Boltzmann model for crystal growth from supersaturated solution, Geophysical Research Letters 31 (2004) L21604.
[20] W.W. Mullins, R.F. Sekerka, Stability of a planar interface during solidification of a dilute binary alloy, Journal of Applied Physics 35 (1964) 444.
[21] W.W. Mullins, R.F. Sekerka, Morphological stability of a particle growing by diffusion or heat flow, Journal of Applied Physics 34 (1963) 323.
[22] M.P. Allen, D.J. Tildesley, Computer Simulation of Liquids, Oxford University Press, Oxford, 2001, p. 81.
[23] R. Courant, K. Friedrichs, H. Levy, Uber die partiellen differenzengleichungen der mathematischen physic, Mathematische Annalen 100 (1928) 32.
[24] J.J. Monoghan, Smoothed particle hydrodynamics, Annual Reviews of Astronomy and Astrophysics 30 (1992) 543.
[25] I.J. Schoenberg, Contributions to the problem of approximation of equidistant data by analytical functions: part A, Quantum Applied Mathematics IV (1946) 45.
[26] L.M. Sander, P. Ramanlal, E. Ben-Jacob, Diffusion limited aggregation as a deterministic growth, Physical Review A32 (1985) 3160.
[27] A.K. Chaniotis, D. Poulikakos, P. Koumoutsakos, Remeshed smoothed particle hydrodynamics for the simulation of viscous and heat conducting flows, Journal of Computational Physics 182 (2002) 67–90.
[28] B.B. Mandelbrot, The Fractal Geometry of Nature, W.H. Freeman, New York, 1984.
[29] T.A. Witten, L.M. Sander, Diffusion limited aggregation, a kinetic critical phenomenon, Physical Review Letters 47 (1981) 1400.
[30] P. Meakin, Fractals, Scaling and Far From Equilibrium, Cambridge University Press, Cambridge, UK, 1998.
[31] P. Meakin, Diffusion-controlled cluster formation in 2–6-dimensional space, Physical Review A27 (1983) 1495–1507.
[32] E. Bouchaud, Scaling properties of cracks, Journal of Physics-Condensed Matter 9 (1997) 4319.
[33] G.S. O'Brien, C.J. Bean, F. McDermott, Numerical investigation of passive and reactive flow through generic single fractures with heterogeneous permeability, Earth and Planetary Science Letters 213 (2003) 271–284.